Journal Name

ARTICLE

Chalcogenide and Pnictide Nanocrystals from the Silylative Deoxygenation of Metal Oxides

Received 00th January 20xx,
Accepted 00th January 20xx

DOI: 10.1039/x0xx00000x

www.rsc.org/

Chia-Cheng Lin,[a,+] Shannon J. Tan[a] and Javier Vela[a,b]*

Transition metal chalcogenide and pnictide nanocrystals are of interest for optoelectronic and catalytic applications. Here, we present a generalized route to the synthesis of these materials from the silylative deoxygenation of metal oxides with trimethylsilyl reagents. Specific nanophases produced in this way include Ni_3S_2, Ni_5Se_5, Ni_2P, Co_9S_8, Co_3Se_4, CoP, Co_2P, and heterobimetallic $(Ni/Co)_9S_8$. The resulting chalcogenide nanocrystals are hollow, likely due to differential rates of ion diffusion during the interfacial phase transformation reaction (Kirkendall-type effect). In contrast, the phosphide nanocrystals are solid, likely because they form at higher reaction temperatures. In all cases, simultaneous partial decomposition of the deoxygenating silyl reagent produces a coating of amorphous silica around the newly formed nanocrystals, which could impact their stability and recyclability.

1. Introduction

Transition metal chalcogenides and pnictides have attracted much interest due to their catalytic and opto-electronic properties.[1] These materials are active in the catalytic upgrading of conventional and bio-derived oils through hydrodesulfurization (HDS), hydrodeoxygenation (HDO), and hydrodenitrification (HDN) reactions.[2-5] As an example, Ni_2P has comparable activity to the Ni-Mo-S catalyst currently used for industrial HDS and HDN.[6] Transition metal chalcogenides and phosphides are also active in water electrolysis. Late transition metal sulfides have been used for electrochemical evolution of oxygen[7,8] and hydrogen.[9-15] Ni_7S_6 is capable of selectively hydrogenating chloronitrobenzene.[16] Furthermore, metal sulfides[17] and phosphides have been employed in lithium ion[18] and aqueous alkaline batteries and solar cells.[19]

To fully understand and utilize these materials and their properties, efforts were devoted to develop synthetic strategies that generate high surface area versions with phase-, morphology- and size-control. Transition metal chalcogenides[20-24] and phosphides[1,25-27] are often made by chemical vapor deposition,[28-29] hydrogen plasma reduction,[30] metal phosphate reduction,[30] reaction of metal chlorides with phosphorous,[32-34] and solution phase decomposition of suitable molecular precursors, including metal-trioctylphosphine complexes[35-38] and metal carbonyl- or acetylacetonate-alkyl phosphine and phosphide complexes.[39-47]

Treatment of preformed metals and metal oxides with elemental sulfur and phosphorus, or with alkyl sulfides and phosphines also produces metal sulfides[48-52] and phosphides.[53-56] These catalytic active materials can then be immobilized in a high surface area, porous solid support in order to increase their stability and recyclability. Silica is a common support as demonstrated recently with metal phosphides,[57] such as Pd_5P_2[58] or Ni_2P/SiO_2.[59-61]

Silylative defluorination and deoxygenation reactions are regularly used in the synthesis and deprotection of molecular inorganic and organic compounds.[62] For example, they have been used in stoichiometric and catalytic C-F bond activation and hydrodefluorination.[63-65] These reactions are driven by the formation of very strong Si–X bonds between silicon and a highly electronegative element, such as F (Si–F, 576 kJ/mol) or O (Si–O, 800 kJ/mol).[66] Here, we explore the use of silylative deoxygenation of *preformed metal oxide nanocrystals* with trimethylsilyl precursors (TMS_xE, where TMS = Me_3Si and $_xE$ = $_2S$, $_2Se$, $_3P$) in order to synthesize nanocrystalline metal phosphides and chalcogenides (Scheme 1). Parallel *in situ* decomposition of excess trimethylsilyl precursor creates a protecting silica shell around the newly formed nanocrystals. Thus, this new methodology results in silica-encapsulated metal chalcogenide and phosphide nanocrystals in a simple, single step synthetic process.

Scheme 1. Silylative deoxygenation of metal oxides.

$$M_2O_x + (TMS)_yE \xrightarrow[Ar]{\Delta} M_yE_x + (TMS)_2O$$

$$TMS = SiMe_3;\quad M = Co, Ni;\quad {}_yE = {}_2S, {}_2Se, {}_3P$$

2. Experimental

2.1 Materials

Cobalt(II) acetylacetonate (acac) ($Co(MeCOCHCOMe)_2$), cobalt(II) acetate tetrahydrate ($(MeCOO)_2Co{\cdot}4H_2O$), Brij 58 (poly(ethylene glycol)hexadecyl ether), tetraethylorthosilicate ($Si(OEt)_4$, TEOS), hexamethyldisilazane ($(CH3)_3SiNHSi(CH_3)_3$, HMDS) and bis(trimethylsilyl) sulfide ($(Me_3Si)_2S$, TMS_2S) were purchased from Sigma-Aldrich; methanol, ethanol (absolute, 200 proof),

[a] Department of Chemistry, Iowa State University, Ames, Iowa, 50011.
[b] Ames Laboratory, Ames, Iowa, 50011.
†Current address: Department of Chemistry, University of Michigan, Ann Arbor, Michigan, 48109.
Electronic Supplementary Information (ESI) available: Additional optical density (absorption + scattering), powder X-ray diffraction, electron microscopy characterization, and ^{29}Si ssNMR data. See DOI: 10.1039/x0xx00000x

isopropanol (2-propanol), cyclohexane, aqueous ammonium hydroxide (28.54 wt%) and diethylamine from Fisher; nickel chloride hexahydrate ($NiCl_2$•$6H_2O$), trioctylphosphine (TOP), bis(trimethylsilyl)selenide ($(Me_2Si)_2Se$, TMS_2Se) and tris(trimethylsilyl)phosphine ($(Me_3Si)_3P$, TMS_3P, 10 wt% in hexane) from Strem; oxalic acid from Alfa Aesar; oleylamine (*Z*-octadec-9-enylamine), sodium borohydride ($NaBH_4$, ≥98%) and hydrazine monohydrate (N_2H_4•H_2O) from Acros. CAUTION: Hydrazine is a hazardous, corrosive and flammable chemical; it is an irritant to skin and by ingestion, eye contact, and inhalation. Hydrazine is explosive in the presence of metals or oxidants. Its use requires well-trained personnel wearing approved personal protective equipment in a well-ventilated environment. Chemicals were used as received unless specified otherwise.

2.2 Material Synthesis

NiO nanocrystals were synthesized according to a slightly modified procedure involving the thermal decomposition of nickel(II) oxalate.[67] An ethanolic 0.3 M oxalic acid solution (25 mL) was gradually added to an ethanolic 0.3 M nickel(II) chloride solution (25 mL) at 50 °C, while stirring for 2 h. Nickel(II) oxalate was collected by concentration under vacuum at 80 °C. Heating nickel oxalate to 400 °C in air for 2 h yielded gray NiO nanocrystals. *$NiO \subset SiO_2$ nanocomposites* were prepared following a procedure we previously reported.[68] *$NiCo_2O_4$ nanocrystals*. A 0.2 M ethanolic solution of nickel(II) acetate (25 mL) was slowly added to a 0.4 M ethanolic solution of cobalt(II) acetate (25 mL). After 2 h of stirring, the transparent solution became cloudy. The solid was collected via vacuum filtration, and dried in an oven at 80 °C. Heating nickel cobalt acetate to 400 °C in air and held for 2 h produced dark $NiCo_2O_4$ nanocrystals. *CoO nanocrystals* were prepared following a slightly modified reported procedure.[69] Briefly, cobalt(II) acetylacetonate (0.14 g, 0.54 mmol), de-ionized water (0.05 g, 2.78 mmol) and oleylamine (7.30 g, 27.3 mmol) were added to a single neck 100 mL round bottom flask connected to a condenser with a glass stopcock adapter. After purging the system with Ar for 20 min, the solution was heated to 210 °C for 1 h. After cooling to room temperature, particles were precipitated by adding excess methanol (several mL) and separated by centrifugation (5,000 rpm, 10 min). The solid (particles) was (were) re-dispersed in hexane and re-precipitated by adding excess amount of ethanol (several mL) followed by centrifugation (5,000 rpm, 10 min). This washing cycle was repeated three times. *Co_3O_4 nanocrystals* were prepared by a slightly modified procedure involving the thermal decomposition of cobalt(II) oxalate.[70] A solution of 0.3 M cobalt acetate in ethanol (50 mL) was heated to 50 °C for 30 min, followed by quick addition of oxalic acid (1.07 g, 11.9 mmol). After 2 h at 50 °C, cobalt(II) oxalate was collected by concentration under vacuum at 80 °C. Heating cobalt(II) oxalate powder to 400 °C in air for 2 h yielded Co_3O_4 nanocrystals. Porous Co_3O_4/SiO_2 core/shell nanoparticles (5 nm thick) were prepared followed a previously reported procedure.[71]

Silylative deoxygenation of metal oxide nanocrystals was performed in a Schlenk line under dry Ar at designated temperatures (see below). An oven-dried three-neck round bottom flask equipped with a PTFE-coated magnetic stir bar, a glass stopcock adapter and a condenser were cooled down and assembled inside a glovebox. *With bis(trimethylsilyl)sulfide*. Metal oxide nanocrystals (10 mg, 134-142 μmol), TMS_2S (0.1 mL, 0.47 mmol) and TOP (2 mL, 4.5 mmol) were added into the flask. After connecting it to the Schlenk line, the flask was evacuated under vacuum and refilled with Ar. The mixture was heated to 130 °C for at least 16 h. During reaction, aliquots (*ca.* 0.2 mL) were taken, washed by precipitation and re-dispersion cycles (see above), and the solid products were analyzed by XRD and optical absorption (below). *With bis(trimethylsilyl)selenide*. Performed under identical conditions as mentioned above for TMS_2S. *With tris(trimethylsilyl)phosphine*. Performed under similar conditions as mentioned above for TMS_2S, except that, due to the increased reactivity of TMS_3P, all glassware had to be surface passivated. Briefly, the oven dried Schlenk tube was allowed to cool down under vacuum, and surface silanol groups were passivated by exposure to hexamethyldisilazane (HMDS) in a low-pressure chamber or desiccator. CAUTION: Trimethylsilyl reagents are toxic, very reactive and, in the case of TMS_3P, flammable and pyrophoric. Only well-trained personnel wearing approved personal protective equipment in an inert environment, such as a dry, oxygen-free glove box should handle these reagents. Silylative deoxygenation products were typically dispersed in organic solvents such as hexanes or toluene.

2.3 Structural Characterization

Powder X-ray diffraction (XRD) data were measured using a Rigaku Ultima IV diffractometer with a Cu Kα radiation source (40 kV, 44 mA). Sample percent composition was determined using PowderCell 2.4 (PCW) refined against standard XRD patterns. *Nitrogen physisorption* was measured on a Micromeritics ASAP 2020 surface area and porosimetry system. Samples were degassed at 100 °C under vacuum overnight prior to the analysis. Surface area was calculated with the Brunauer-Emmett-Teller (BET) method in the relative pressure range of 0.005 to 0.25 of adsorption data. Pore size distribution was calculated with the Barret-Joyber-Halenda (BJH) method. *Transmission Electron Microscopy* (TEM) was measured on an FEI Tecnai G^2 F20 field emission scanning transmission electron microscope (S/TEM) at 200 kV (point-to-point resolution <0.25 nm, line-to-line resolution <0.10 nm).

2.4 Spectroscopic Characterization

Solution-phase optical density (absorption + scattering) spectra (UV-Vis) were collected in toluene with a photodiode-array Agilent 8453 UV–Vis spectrophotometer. Solid state NMR data were collected with a Bruker Avance II 600 spectrometer at 119.2 MHz for ^{29}Si equipped with a 4 mm Bruker MAS probe spinning at 10 KHz. ^{29}Si DP-MAS NMR spectra were recorded with a pulse width of 4 μs and a recycling delay of 1 min. ^{29}Si NMR spectra were externally referenced to siloxane (δ = -9.6 ppm), and ^{29}Si isotropic chemical shifts reported against TMS (δ = 0 ppm).

3. Results and Discussion

Silylative deoxygenation of bare nickel oxide. Silylative deoxygenation of cubic, rock salt NiO nanocrystals with TMS_2S in trioctylphosphine (TOP) for 20 h at 130 °C results in a noticeable color change from light gray to black (Scheme 2a). This is consistent with the appearance of a broad light absorption hump in the 400-1000 nm region (Figure 1). Powder X-ray diffraction (XRD) is consistent with formation of Ni_3S_2 (Figure 2), indicating partial reduction of Ni(II) to Ni(I). Transmission electron microscopy (TEM) and high-angle annular dark-field scanning transmission electron microscopy (HAADF-STEM) show the newly formed Ni_3S_2 nanocrystals possess a distinct hollow morphology, with an overall average particle diameter of 36±7 nm and an average Ni_3S_2 'shell' thickness of 8±2 nm. The latter is close to the average Ni_3S_2 single crystalline domain size of 13±3 nm calculated from XRD peak widths using the Scherrer equation (Table 1). The hollow Ni_3S_2 nanocrystals appear to be coated with an outer, amorphous silica (SiO_2) shell

(Figure 3c). In fact, TEM of all nanocrystals produced by silylative deoxygenation reveals the presence of a lower contrast outer layer which originates from decomposition of excess trimethylsilyl reagent into amorphous silica (SiO_2). This is confirmed by ^{29}Si solid state (ss) NMR measurements. For example, the ^{29}Si ssNMR spectra of Ni_3S_2/SiO_2 and Co_9S_8/SiO_2 (see below) show a broad resonance around -100 ppm, which is consistent with partly merging Q bands (Q^2, Q^3 and Q^4)—see Supporting Information (SI).[71]

Scheme 2. Silylative deoxygenations of NiO (unbalanced).

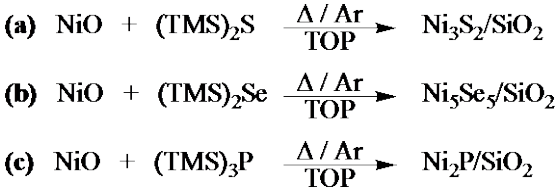

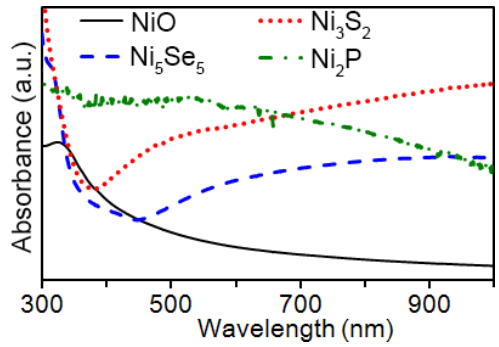

Figure 1. Solution-phase optical density of NiO nanocrystals before and after silylative deoxygenation.

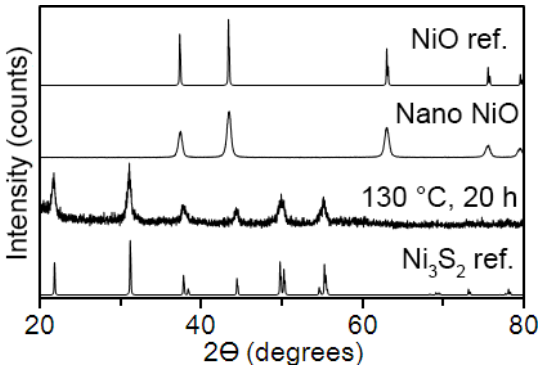

Figure 2. Powder XRD patterns of NiO nanocrystals and the product of silylative deoxygenation with TMS_2S. Reported XRD patterns for bulk rock salt NiO and heazlewoodite Ni_3S_2 are shown for comparison.

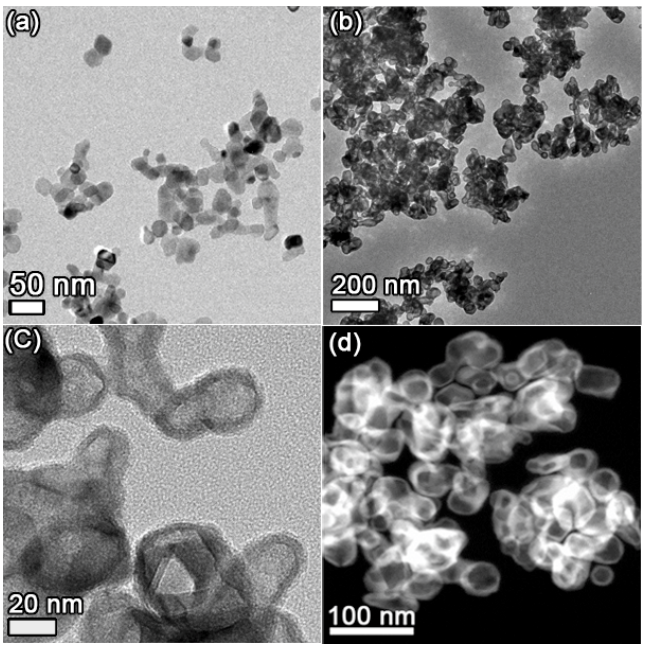

Figure 3. Representative bright field TEM images of NiO (a), the product of silylative deoxygenation with TMS_2S (b, c). HAADF-STEM image of the latter (d).

Silylative deoxygenation of NiO nanocrystals with TMS_2Se in TOP for 20 h at 130 °C (Scheme 2b) results in a similar color change and chemical transformation (Figure 1). Powder XRD and TEM data reveal formation of hollow Ni_5Se_5 particles with total and shell dimensions of 36±7 nm and 7±2 nm, respectively. Thus, unlike the sulfide case, the oxidation state of Ni(II) remains unchanged in the product. As before, an amorphous SiO_2 shell is clearly visible, which likely arises from thermal decomposition of excess silyl reagent.

Silylative deoxygenation of NiO nanocrystals with TMS_3P in TOP at 250 °C for 17 h (Scheme 2c) results in a color change from light gray to dark gray, as evidenced by the appearance of a broad absorption between 500-900 nm (Figure 1). Importantly, control experiments in the absence of TMS_3P unambiguously show that TOP does NOT act as a source of phosphide under the same reaction conditions. When TMS_3P is added, powder XRD and TEM analyses confirm formation of 'solid' (not void/not hollow) Ni_2P nanocrystals, with Scherrer and TEM diameters of 11±1 nm and 12±2 nm, respectively (Figures 4 and 5). Thus, Ni(II) is partially reduced to Ni_2P. TEM and HAADF-STEM reveal the Ni_2P nanocrystals are embedded inside an amorphous silica (SiO_2) matrix. Thus, part of the driving force for silylative deoxygenation comes from formation of very strong Si-O bonds, not only in free TMS_2O (Scheme 1), but also in the amorphous SiO_2 overlayer coating the resulting particles (Scheme 2).

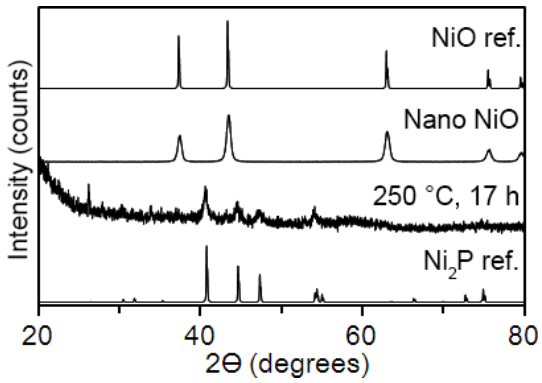

Figure 4. Powder XRD patterns of NiO nanocrystals and the product of silylative deoxygenation with TMS_3P. Reported XRD patterns for bulk rock salt NiO and Mn_2P-type Ni_2P are shown for comparison.

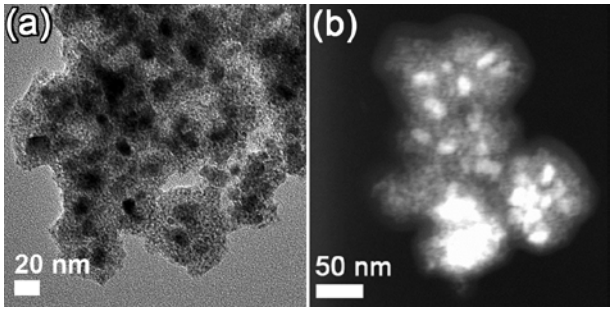

Figure 5. Representative bright field TEM (a) and HAADF-STEM (b) images of Ni_2P nanocrystals produced by silylative deoxygenation of NiO with TMS_3P.

Understanding hollow vs. solid nanocrystal formation. Formation of vesicle-like chalcogenide nanoparticles is consistent with a Kirkendall-type effect.[15,35,36,42,48,50,56] Reactions at solid–liquid interfaces are affected by relative diffusion rates of the different ions involved. When the diffusion rate of the reacting ('inner') material (NiO) is greater than that of the newly produced ('outer') material (Ni_3S_2), a net outward mass flow results that is accompanied by an inward void or 'vacancy' flow; in the most extreme case, this can lead to shell cracking and fragmentation, leading to small nanoparticles (Scheme 3). During the first two interfacial silylative deoxygenation reactions above, the smaller oxide anion (O^{2-}) diffuses out of the nanocrystal and onto its surface much faster than the heavier and larger sulfide anion (S^{2-}) diffuses into the new lattice.[54] Further, the highly oxophilic Si center in TMS_2Si is expected to act as an avid oxide sponge at the surface of the original NiO nanoparticles, accelerating the outward mass flow.

Scheme 3. Kirkendall-type hollowing and fragmentation during silylative deoxygenation of metal oxide nanocrystals.

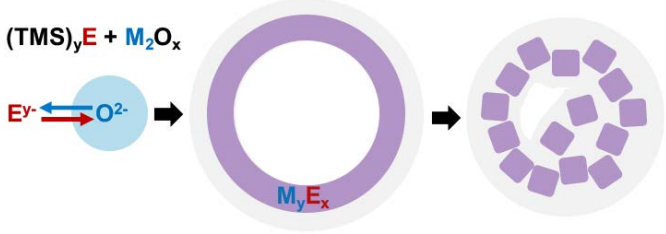

The absence of similar voids in Ni_2P nanocrystals could be discussed in the context of several factors, including relative anion charge, size, polarizability, metal–element bond strength, specific lattice entropy, or reaction temperature. It is well known that diffusion of ions in solids increases as ionic size, charge and metal-element bond strength decrease. Thus, formation of voids in hollow nickel sulfides and selenides can be explained on the basis of the expected relative diffusion rates: $O^{2-} > S^{2-} > Se^{2-}$. However, the absence of voids in nickel phosphide is counterintuitive based on the expected relative diffusion rates: $O^{2-} > S^{2-} > P^{3-}$ (this would imply the nickel phosphide particles should have the most pronounced voids, which is not observed). Stronger nickel-phosphide bonds, or higher reaction temperature required for silylative deoxygenation, or both may explain the lack of voids in Ni_2P. In particular, the higher reaction temperatures could minimize or cancel out any differential diffusion rates of both outward-bound O^{2-} ions and inward-bound P^{3-} across the solid-liquid interface. Additionally, a higher reaction temperature could also cause any initially formed (and otherwise observable) void to collapse due to melting and coalescence of nanosized particles.[68] The higher reaction temperature may also be responsible for the formation of a much thicker, more distinct silica outer matrix, due to increased thermal decomposition of excess trimethylsilyl reagent (when using TMS_3P *vs.* TMS_2S and TMS_2Se).

Silylative deoxygenation of bare cobalt oxides. Silylative deoxygenation of deep black Co_3O_4 nanocrystals with TMS_2S in TOP for 25 h at 130 °C (Scheme 3a) occurs without a significant color change. Powder XRD and TEM data show formation of a mixture of CoO and Co_9S_8, hollow nanocrystals (see SI). Thus, this reaction is accompanied by partial reduction of Co(III) to Co(II). Similarly, silylative deoxygenation of Co_3O_4 nanocrystals with TMS_2Se in TOP for 20 h at 130 °C (Scheme 3c) did not result in a significant color change. Powder XRD and TEM show formation of a mixture of CoO and Co_3Se_4, hollow nanocrystals (see SI). In contrast, silylative deoxygenation of CoO nanocrystals with TMS_2S in TOP for 20 h at 130 °C (Scheme 3b) results in a color change from brown to black, as evidenced by loss of the two 600 nm and 700 nm peaks in the solution-phase absorption spectrum (Figure 6a). Powder XRD and TEM show formation of hollow Co_9S_8 nanocrystals with an overall average particle diameter of 20±3 nm and an average Co_9S_8 shell thickness of 8±2 nm (Figures 7 and 8). The latter is close to the average Co_9S_8 single crystalline domain size of 6±1 nm calculated from XRD peak widths using the Scherrer equation (Table 1).

Scheme 4. Silylative deoxygenations of Co_xO_y (unbalanced).

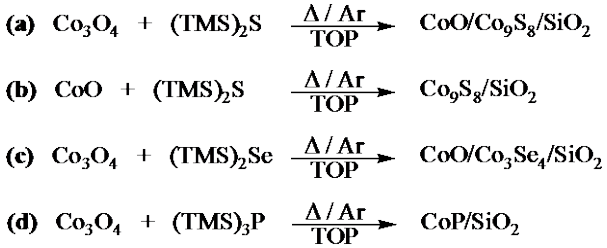

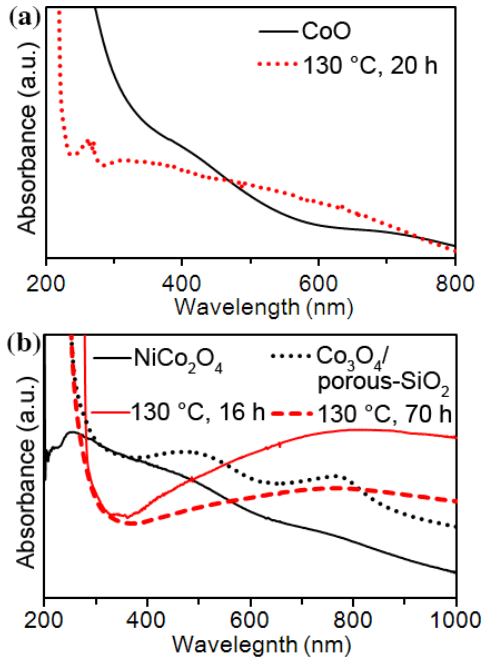

Figure 6. Solution-phase optical density of before and after silylative deoxygenation with TMS_2S of CoO (a), $NiCO_2O_4$, and Co_3O_4/porous-SiO_2 nanocrystals (b).

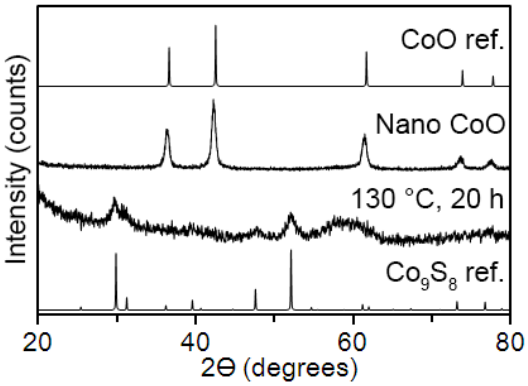

Figure 7. Powder XRD patterns of CoO nanocrystals and the product of silylative deoxygenation with TMS_2S. Reported XRD patterns for bulk rock salt CoO and cobalt pentlandite Co_9S_8 are shown for comparison.

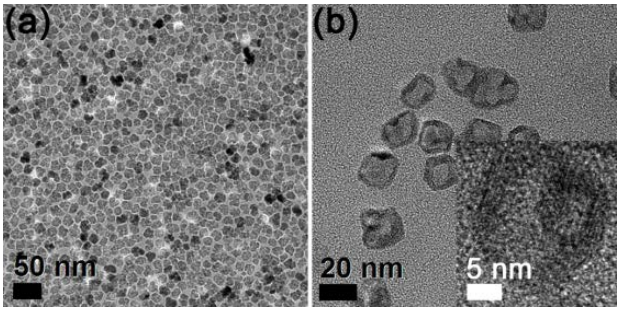

Figure 8. Representative TEM images of CoO (a) and Co_9S_8 nanocrystals from silylative deoxygenation with TMS_2S (b).

Silylative deoxygenation of Co_3O_4 with TMS_3P in TOP for 17 h at 250 °C (Scheme 3d) results in a color change from black to dark gray, as evidenced by disappearance of the 500 nm and 800 nm absorption peaks (see SI). As in the nickel case above, powder XRD and TEM show formation of solid CoP nanocrystals with single crystalline and overall sizes of 6±1 nm and 11±3 nm, respectively. These are clearly embedded in an amorphous silica layer (Figure 9). Interestingly, low Co to P ratios yield CoP, while higher Co to P ratios yield a mixture of Co_2P and CoP (see SI). Thus, silylative deoxygenation proceeds with partial reduction of Co(III and II, in Co_3O_4 spinel) to Co_2P. Also as in the nickel case, no phosphides formed in the absence of TMS_3P, demonstrating that TOP is not a source of phosphide under our reaction conditions.

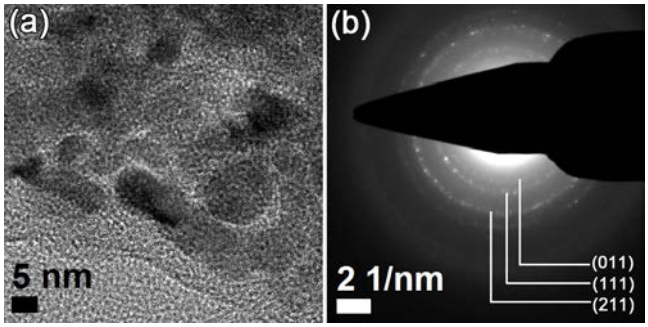

Figure 9. Representative TEM image (a) and selected area electron diffraction pattern (b) of CoP/SiO_2 nanocrystals produced by silylative deoxygenation of Co_3O_4 with TMS_3P.

Silylative deoxygenation of mixed-metal oxides. Having established the wide generality of silylative deoxygenation reactions from simple and readily available metal oxide precursors, we probed whether they could be applied to mixed-metal oxides. In particular, we questioned whether silylative deoxygenation could proceed at comparable rates for different metal ions, or if instead it would lead to phase segregation. To test this idea, we performed the silylative deoxygenation of $NiCo_2O_4$ nanocrystals with TMS_2S in TOP for 16 h at 130 °C (Scheme 4a). This resulted in a color change from dark gray to black, as evidenced by the loss of 500 nm and 800 nm peaks in the solution-phase absorption spectrum (Figure 6b). Powder XRD, TEM and HAADF-STEM confirm the formation of hollow (Kirkendall-type) nanocrystals with general composition $(Ni/Co)_9S_8$ (Figure 10 and SI). To gain a deeper insight into this reaction, we performed energy dispersive X-ray spectroscopy (EDS) mapping, which reveals Co (K- and L-edge), Ni (K- and L-edge) and S (K-edge) are distributed homogeneously across particles (Figure 11). EDS elemental analysis of different areas containing several nanocrystals showed Co to Ni ratios between 8 and 5, which agrees with two well-known mixed-metal sulfide phases: $NiCo_8S_8$ and $Ni_3Co_6S_8$ (Table 1). These results demonstrate that silylative deoxygenation of more complex, mixed-metal oxides can also occur without significant phase segregation.

Scheme 5. Silylative deoxygenations of mixed-metal and silica-coated metal oxides (unbalanced).

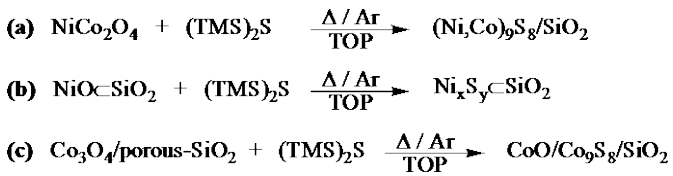

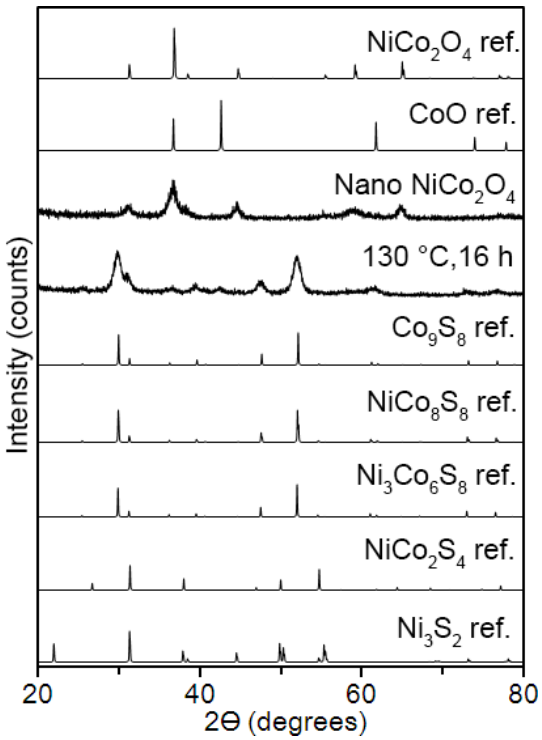

Figure 10. Powder XRD patterns of $NiCo_2O_4$ nanocrystals before and after silylative deoxygenation with TMS_2S. Reported patterns for several relevant oxides and sulfides are shown for comparison.

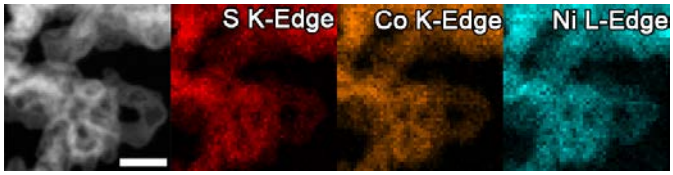

Figure 11. Registered HAADF-STEM/EDS images of the product of silylative deoxygenation of $NiCo_2O_4$ with TMS_2S. Scale bar = 50 nm.

Silylative deoxygenation of silica-coated metal oxides. Finally, we tested the feasibility of performing silylative deoxygenation of nanocrystalline metal oxides that are already contained in a protective silica matrix. NiO nanocrystals embedded in one-dimensional 'solid'—non-porous—silica capsules ($NiO \subset SiO_2$) react with TMS_2S in TOP for 70 h at 130 °C (Scheme 4b) to give a mixture of $Ni_3S_2/Ni_9S_8 \subset SiO_2$ (see SI). It is not surprising then, that silylative deoxygenation of embedded in porous silica shells (Co_3O_4/porous-SiO_2 core/shells) react with TMS_2S under similar conditions to give a mixture of $CoO/Co_9S_8/SiO_2$ (Figure 6b and SI). Thus, silylative deoxygenation of metal oxides generally produces—and proceeds through—high surface-area, silica coated nanomaterials, which could enable their use and recycling in catalytic and other technologically-relevant applications.[1,20-27]

Conclusions

In summary, we have successfully demonstrated the versatility of utilizing trimethylsily reagents (TMS_xE) to transform preformed, nanocrystalline metal oxides (NiO, Co_3O_4, CoO, and $NiCo_2O_4$) into nanocrystalline metal chalcogenides and pnictides. Nanocrystalline phases produced via this silylative deoxygenation reaction include Co_9S_8, Co_3Se_4, CoP, Co_2P, Ni_3S_2, Ni_5Se_5 and Ni_2P. Nanocrystalline chalcogenide (sulfides, selenides) resulting from silylative deoxygenation possess hollow, vesicle like morphologies, whereas the nanocrystalline pnictides (phosphides) do not. Hollow morphologies can be explained on the basis of a nanoscale Kirkendall-type effect, arising from differential ion diffusion rates between ions in the reactant and product phases.

The silylative deoxygenation route presented here nicely complements other published methods that are available for the synthesis of metal chalcogenide and pnictide nanocrystals. All nanocrystalline chalcogenides and pnictides produced by silylative deoxygenation are surrounded by an outer amorphous silica layer, which could help in preventing agglomeration and degradation. Introduction of porosity within these shells may be accomplished by adding a surfactant during the silylative deoxygenation process. Successful silylative deoxygenation of the ternary, mixed-metal oxide $NiCo_2O_4$ with TMS_2S demonstrates that silylative deoxygenation can be performed from more complex precursors without significant phase segregation. This could enable the preparation of ternary systems, such as II-IV-VI semiconductors (e.g., $CaTiS_3$, $BaZrS_3$, $CaZrSe_3$) from well-known metal oxides, and for which traditional routes remain underdeveloped. Similarly, successful silylative deoxygenation of silica-encapsulated metal oxides bears potential in particle recycling and regeneration.

Acknowledgements

J. Vela thanks the U.S. National Science Foundation for a CAREER grant from the Division of Chemistry, Macromolecular, Supramolecular and Nanochemistry program (1253058). Electron microscopy was performed at Ames Laboratory's Sensitive Instrument Facility. Ames Laboratory is operated for the U.S. Department of Energy by Iowa State University under Contract DE-AC02-07CH11358. The authors thank Bryan Rosales, Aaron Sadow, Art White, Sarah Cady, and Himashi Andaraarachchi for comments.

References

1. S. Carenco, D. Portehault, C. Boissière, N. Mézailles, C. Sanchez, *Chem. Rev.*, 2013, **113**, 7981.
2. R. Prins, M. E. Bussell, *Catal. Lett.*, 2012, **142**, 1413.
3. H. Zhao, D. Li, P. Bui, S. T. Oyama, *Appl. Catal., A*, 2011, **391**, 305.
4. S.-K. Wu, P.-C. Lai, Y.-C. Lin, H.-P. Wan, H.-T. Lee, H.-T. Chang, *ACS Sustain. Chem. Eng.*, 2013, **1**, 349.
5. A. W. Burns, K. A. Layman, D. H. Bale, M. E. Bussell, *Appl. Catal., A*, 2008, **343**, 68.
6. T. S. Oyama, T. Gott, H. Zhao, Y.-K. Lee, *Catal. Today*, 2009, **143**, 94.
7. M. Gao, J. Jiang, S. Yu, Small, 2012, *8*, 13.
8. R. A. Sidik, A. B. Anderson, *J. Phys. Chem. B*, 2006, **110**, 936.
9. C. Di Giovanni, W.-A. Wang, S. Nowak, J.-M. Grenèche, H. Lecoq, L. Mouton, M. Giraud, C. Tard, *ACS Catal.*, 2014, **4**, 681.
10. Y. Xu, M. Gao, Y. Zheng, J. Jiang, S. Yu, *Angew. Chem., Int. Ed.*, 2013, **33**, 8546.

11. D. Kong, H. Wang, Z. Lu, Y. Cui, *J. Am. Chem. Soc.*, 2014, **136**, 4897.
12. Y. Sun, C. Liu, D. C. Grauer, J. Yano, J. R. Long, P. Yang, C. J. Chang, *J. Am. Chem. Soc.*, 2013, **135**, 17699.
13. J. Xie, J. Zhang, S. Li, F. Grote, X. Zhang, H. Zhang, R. Wang, Y. Lei, B. Pan, Y. Xie, *J. Am. Chem. Soc.*, 2013, **135**, 17881.
14. J. Tian, Q. Liu, A. Asiri, X. Sum, *J. Am. Chem. Soc.*, 2014, **136**, 7587.
15. E.J. Popczun, J.R. McKone, C.G. Read, A.J. Biacchi, A.M. Wiltrout, N.S. Lewis, R.E. Schaak, *J. Am. Chem. Soc.*, ,2013, **135**, 9267.
16. F. Cao, R. X. Lin, L. Zhou, S. Y. Song, Y. Q. Lei, W. D. Shi, F. Y. Zhao, H. J. Zhang, *J. Mater. Chem.*, 2010, **20**, 1078.
17. C.-H. Lai, M.-Y. Lu, L.-J. Chen, *J. Mater. Chem.*, 2012, **22**, 19.
18. D. Yang, J. Zhu, X. Rui, H. Tan, R. Cai, H. E. Hoster, D. Y. W. Yu, H. H. Hng, Q. Yan, *ACS Appl. Mater. Interfaces*, 2013, **5**, 1093.
19. S.-H. Chang, M.-D. Lu, Y.-L. Tung, H.-Y. Tuan, *ACS Nano*, 2013, **7**, 9443.
20. P. Reiss, M. Carrière, C. Lincheneau, L. Vaure, S. Tamang, *Chem. Rev.*, 2016, **116**, 10731.
21. J. van Embden, A. S. R. Chesman, J. J. Jasieniak, *Chem. Mater.*, 2015, **27**, 2246.
22. J. Chang, E. R. Waclawik, *RSC Adv.*, 2014, **4**, 23505.
23. M.-R. Gao, Y.-F. Xu, J. Jiang, S.-H. Yu, *Chem. Soc. Rev.*, 2013, **7**, 2986.
24. S. V. Kershaw, A. S. Susha, A. L. Rogach, *Chem. Soc. Rev.*, 2013, **42**, 3033.
25. Y. M. Shi, B. Zhang, *Chem. Soc. Rev.*, 2016, **45**, 1529.
26. Carenco, D. Portehault, C. Boissière, N. Mézailles, C. Sanchez, *Adv. Mater.* 2014, **26**, 371.
27. J. F. Callejas, C. G. Read, C. W. Roske, N. S. Lewis, R. E. Schaak, *Chem. Mater.* 2016, **28**, 6017.
28. A. Panneerselvam, M. A. Malik, M. Afzaal, P. O'Brien, M. Helliwell, *J. Am. Chem. Soc.*, 2008, **130**, 2420.
29. W. Maneeprakorn, M.A. Malik, P. O'Brien, *J. Mater. Chem.*, 2010, **20**, 2329.
30. A. J. Wang, M. L. Qin, J. Guan, L. Wang, H. C. Guo, X. Li, Y. Wang, R. Prins, Y. K. Hu, *Angew. Chem., Int. Ed.*, 2008, **47**, 6052.
31. K. L. Stamm, J. C. Garno, G.-y. Liu, S. L. Brock, *J. Am. Chem. Soc.*, 2003, **125**, 4038.
32. Y. Xie, H. L. Su, X. F. Qian, X. M. Liu, Y. T. Qian, *J. Solid State Chem.*, 2000, **149**, 88.
33. B. M. Barry, E. G. Gillan, *Chem. Mater.*, 2009, **21**, 4454.
34. S. Carenco, Y. Hu, I. Florea, O. Ersen, C. Boissière, N. Mézailles, C. Sanchez, *Chem. Mater.*, 2012, **24**, 4134.
35. A. E. Henkes, Y. Vasquez, R. E. Schaak, *J. Am. Chem. Soc.*, 2007, **129**, 1896.
36. R. K. Chiang, R. T. Chiang, *Inorg. Chem.*, 2007, **46**, 369.
37. J. Park, B. Koo, Y. Hwang, C. Bae, K. An, J.-G. Park, H. M. Park, T. Hyeon, *Angew. Chem., Int. Ed.*, 2004, **43**, 2282.
38. J. Park, B. Koo, K.-Y. Yoon, Y. Hwang, M. Kang, J. G. Park, T. Hyeon, *J. Am. Chem. Soc.*, 2005, **127**, 8433.
39. C. Qian, F. Kim, L. Ma, F. Tsui, P. Yang, J. Liu, *J. Am. Chem. Soc.*, 2004, **126**, 1195.
40. K. A. Gregg, S. C. Perera, G. Lawes, S. Shinozaki, S. L. Brock, *Chem. Mater.*, 2006, **18**, 879.
41. J. Wang, A. C. Johnston-Peck, J. B. Tracy, *Chem. Mater.*, 2009, **21**, 4462.
42. E. Muthuswamy, G. H. L. Savithra, S. L. Brock, *ACS Nano*, 2011, **5**, 2402.
43. K. Mandel, F. Dillon, A. A. Koos, Z. Aslam, K. Jurkschat, F. Cullen, A. Crossley, H. Bishop, K. Moh, C. Cavelius, E. Arzt, N. Grobert, *Chem. Commun.*, 2011, **47**, 4108.
44. H. Zhang, D.-H. Ha, R. Hovden, L.F. Kourkoutis, R. D. Robinson, *Nano Lett.*, 2011, **11**, 188.
45. S. C. Perera, G. Tsoi, L. E. Wenger, S. L. Brock, *J. Am. Chem. Soc.*, 2003, **125**, 13960.
46. D. K. Harris, M. G. Bawendi, *J. Am. Chem. Soc.*, 2012, **134**, 20211.
47. S. Joung, S. Yoon, C.-S. Han, Y. Kim, S. Jeong, *Nanoscale Res. Lett.*, 2012, **7**, 93.
48. Y. Yin, C. K. Erdonmez, A. Cabot, S. Hughes, A. P. Alivisatos, *Adv. Funct. Mater.*, 2006, **16**, 1389.
49. C. J. Chen, R. K. Chiang, *Dalton Trans.*, 2011, **40**, 880.
50. J. Park, H. M. Zheng, Y. W. Jun, A. P. Alivisatos, *J. Am. Chem. Soc.*, 2009, **131**, 13943.
51. H. Zhang, L. V. Solomon, D. H. Ha, S. Honrao, R. G. Hennig, R. D. Robinson, *Dalton Trans.*, 2013, **42**, 12596.
52. Z. Qin, H. Sun, Z. Jiang, X. Jiao, D. Chen, *CrystEngComm*, 2013, **15**, 897.
53. I. T. Sines, R. E. Schaak, *J. Am. Chem. Soc.*, 2011, **133**, 1294.
54. E. Muthuswamy, S. L. Brock, *J. Am. Chem. Soc.*, 2010, **132**, 15849.
55. D.-H. Ha, L. M. Moreau, C. R. Bealing, H. Zhang, R. G. Hennig, R. D. Robinson, *J. Mater. Chem.*, 2011, **21**, 11498.
56. E. Muthuswamy, S. L. Brock, *Chem. Commun.*, 2011, **47**, 12334.
57. C. M. Lukehart, S. B. Milne, S. R. Stock, *Chem. Mater.*, 1998, **10**, 903.
58. G. H. L. Savithra, R. H. Bowker, R. B. A. Carrillo, M. E. Bussell, S. L. Brock, *ACS Appl. Mater. Interfaces*, 2013, **5**, 5403.
59. G. H. L. Savithra, R. H. Bowker, B. A. Carrillo, M. E. Bussell, S. L. Brock, *Chem. Mater.*, 2013, **25**, 825.
60. Y. Yang, C. Ochoa-Hernandez, V. A. de la Peña O'Shea, J. M. Coronado, D. P. Serrano, *ACS Catal.*, 2012, **2**, 592.
61. T. I. Korányi, Z. Vít, D. G. Poduval, R. Ryoo, H. S. Kim, E. J. M. Hensen, *J. Catal.*, 2008, **253**, 119.
62. P. G. M. Wuts, T. W. Greene, *Greene's Protective Groups in Organic Synthesis*, 4th ed.; John Wiley & Sons: New York, **2006**.
63. J. Vela, J. M. Smith, Y. Yu, N. A. Ketterer, C. J. Flaschenriem, R. J. Lachicotte, P. L. Holland, *J. Am. Chem. Soc.*, 2005, **127**, 7857.
64. H. Amii, K. Uneyama, *Chem. Rev.*, 2009, **109**, 2119.
65. J. Y. Corey, *Chem. Rev.*, 2011, **111**, 863.
66. Y.-R. Luo, J.-P. Cheng, Dissociation Energies. In *CRC Handbook of Chemistry and Physics*, 95th ed.; Haynes, W. M., Ed.; Taylor and Francis: Boca Raton, FL, **2014**; Internet Version, 9-65–9-96.
67. X. Wang, J. Song, L. Gao, J. Jin, H. Zheng, Z. Zhang, *Nanotechnology*, 2005, **16**, 37.
68. N. C. Nelson, T. P. A. Ruberu, M. D. Reichert, J. Vela, *J. Phys. Chem. C*, 2013, **117**, 25826.
69. J. H. Shim, K. M. Nam, W. S. Seo, H. Song, J. T. Park, *Chem. Asian J.*, 2011, **6**, 1575.
70. I. Luisetto, F. Pepe, E. Bemporad, *J. Nanopart. Res.*, 2008, **10**, 59.
71. C.-C. Lin, Y. Guo, J. Vela, *ACS Catal.*, 2015, **5**, 1037.

Journal Name

ARTICLE

Table 1. Summary of the Metal Oxide Silylative Deoxygenation Reactions.

#	Precursor	Conditions[d]	Product(s) (%)[f]	XRD Size[h]	TEM Size (o.d.,[i] thickness[j])
1	NiO[a]	TMS_2S/130 °C/20 h/Ar	Hollow Ni_3S_2	13±3 nm	36±7 nm, 8±2 nm
2	NiO[a]	TMS_2Se/130 °C/20 h/Ar	Hollow Ni_5Se_5	7±2 nm	31±7 nm, 7±2 nm
3	NiO[a]	TMS_3P/250 °C/17 h/Ar	Ni_2P	11±2 nm	12±2 nm
4	CoO[b]	TMS_2S/130 °C/20 h/Ar	Hollow Co_9S_8	6±1 nm	20±3 nm, 5±1 nm
5	Co_3O_4[c]	TMS_2S/280 °C/20 h/Ar	Co_9S_8	5±1 nm	n.d.[g]
6	Co_3O_4[c]	TMS_2Se/130 °C/20 h/Ar (Co/P = 0.5)[e]	CoO (n.d.)[d] + hollow Co_3Se_4 (n.d.)[d]	Co_3Se_4: *ca.* 2-3 nm CoO: 15±3 nm	18±5 nm, 7±2 nm
7	Co_3O_4[c]	TMS_3P/250 °C/17 h/Ar (Co/P = 0.5)[e]	CoP	6±1 nm	11±3 nm
8	Co_3O_4[c]	TMS_3P/250 °C/17 h/Ar (Co/P = 1)[e]	CoO (25%)[f] + CoP (44%)[f] + Co_2P (31%)[f]	CoO: *ca.* 7-12 nm CoP: *ca.* 7-8 nm Co_2P: *ca.* 8 nm	n.d.[g]
9	$NiCo_2O_4$[d]	TMS_2S/130 °C/16 h/Ar	Hollow $Ni_xCo_yS_8$ (x = 1-3, y = 8-6)	6.6±0.4 nm	18±5 nm, 6±1 nm
10	$NiO \subset SiO_2$[d]	TMS_2S/130 °C/70 h/Ar	NiO (n.d.)[d] + Ni_3S_2 (n.d.)[d] + Ni_9S_8 (n.d.)[d]	n.d.[g]	n.d.[g]
11	Co_3O_4/SiO_2[d]	TMS_2S/130 °C/70 h/Ar	CoO (30%)[f] + hollow Co_9S_8 (70%)[f]	CoO: 10±1 nm Co_9S_8: 5.7±0.3 nm	n.d.[g]

[a]14.1±0.4 nm. [b]13±2 nm. [c]17±4 nm. [d]See Experimental for full details. [e]Co/P ratio determined by dividing three times the chemical amount of Co_3O_4 over that of TMS_3P (both in moles). [f]Determined by Powder Cell for Windows (PCW). [g]n.d. = Not determined. [h]Measures single crystalline domain size. [i]Outer diameter (total size). [j]Shell thickness (if hollow).

TOC Graphic:

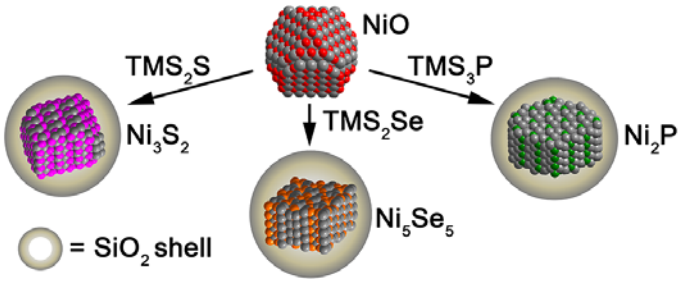

TOC Synopsis:

Transition metal chalcogenides and pnictides are interesting inorganic materials for optoelectronic and catalytic applications. We present a generalized synthesis route to transform preformed metal oxide nanocrystals into sulfides, selenides, or phosphide nanocrystals *via* silylative deoxygenation with highly reactive trimethylsilyl reagents. In all of the reactions studied, simultaneous decomposition of excess silyl reagent produces a protective, amorphous silica coating around the newly formed chalcogenide and pnictide nanocrystals.